Supplementary Information for

RB loss modulates chromatin organization by regulating cohesin-dependent loops and enhancer-promoter interactions

Hanjun Lee*, Ioanna-Maria Gkotinakou*, Connor G. McGrath, Badri Krishnan, Sambhavi Animesh, Isabella Salinas, Robert Morris, Moshe Sade-Feldman, Wilhelm Hass, Michael S. Lawrence†, Ioannis Sanidas†‡

*These authors contributed equally to this work.

†Correspondence: mslawrence@mgh.harvard.edu (M.S.L.), isanidas@mgh.harvard.edu (I.S.)

The PDF file includes:

Supplementary Tables 1 and 2
Supplementary Figs. 1 to 28

Supplementary Table 1. List of antibodies utilized for the study

Antibodies	SOURCE	IDENTIFIER
anti-DYKDDDDK tag	Cell Signaling Technology	Cat. # 14793 RRID: AB_2572291
anti-FLAG (M5)	Sigma-Aldrich	Cat. # F4042 RRID: AB_439686
anti-RB	Cell Signaling Technology	Cat. # 9309S RRID: AB_10696874
anti-H3K4me3	Cell Signaling Technology	Cat. # 9751 RRID: AB_2616028
anti-H3K4me1	Abcam	Cat. # ab8895 RRID: AB_306847
anti-H3K27ac	Active Motif	Cat. # 39034 RRID: AB_2722569
anti-H3K27ac	Cell Signaling Technology	Cat. # 8173 RRID: AB_10949503
anti-H3K27me3	Cell Signaling Technology	Cat. # 12158 RRID: AB_2797834
anti-E2F1	Cell Signaling Technology	Cat. # 3742 RRID: AB_2096936
anti-CTCF	Cell Signaling Technology	Cat. # 3418 RRID: AB_2086791
anti-c-Jun	Cell Signaling Technology	Cat. # 9165 RRID: AB_2130165
anti-SMC3	Abcam	Cat. # ab9263 RRID: AB_307122
anti-acSMC3 K105/K106	Sigma-Aldrich	Cat. # MABE1073
anti-α-tubulin	Sigma-Aldrich	Cat. # T9026 RRID: AB_477593

Supplementary Table 2. List of software utilized for the study

Software	SOURCE	IDENTIFIER
OriginPro (v2023b)	Origin Lab	https://www.originlab.com/
FCS Express (v7.18.0025)	De Novo Software	https://denovosoftware.com/
MATLAB (vR2018b or vR2023a)	MathWorks	https://www.mathworks.com/products/matlab.html
MATLAB Runtime (v9.5)	MathWorks	https://www.mathworks.com/products/compiler/matlab-runtime.html
Perl (v5.30.0)	Larry Wall	https://www.perl.org/
Python (v2.7.18 and v3.8.10)	Python Software Foundation	https://www.python.org/
get_qc.py	Dovetail Genomics	https://github.com/dovetail-genomics/Micro-C
NumPy (v1.22.3)	N/A	https://numpy.org/
Pandas (v1.5.2)	N/A	https://pandas.pydata.org/
Seaborn (v0.11.1)	N/A	https://seaborn.pydata.org/
Matplotlib (v3.4.2)	N/A	https://matplotlib.org/
Bioframe (v0.3.3)	Open2C	https://doi.org/10.1101/2022.02.16.480748
R (v4.3.0)	N/A	https://www.r-project.org/
tximportData (v1.28.0)	Michael Love	https://doi.org/10.18129/B9.bioc.tximportData
tximport (v1.28.0)	Michael Love	https://doi.org/10.18129/B9.bioc.tximport
readr (v2.1.4)	Jennifer Bryan	https://readr.tidyverse.org/
DESeq2 (v1.40.2)	Michael Love	https://doi.org/10.1186/s13059-014-0550-8
Integrative Genomics Viewer (v2.16.2)	Jill P. Mesirov Lab	https://igv.org/
trim-galore (v0.6.4_dev)	Barbraham Bioinformatics	https://www.bioinformatics.babraham.ac.uk/projects/trim_galore/
cutadapt (v2.8)	Sven Rahmann Lab	http://doi.org/10.14806/ej.17.1.200

FastQC (v0.11.9)	Barbraham Bioinformatics	https://www.bioinformatics.babraham.ac.uk/projects/fastqc/
bwa (v0.7.17-r1198-dirty or v0.7.17-r1188)	Richard Durbin Lab	https://doi.org/10.48550/arXiv.1303.3997
bowtie (v2.3.5.1)	Ben Langmead Lab	https://doi.org/10.1038/nmeth.1923
sambamba (v0.7.1)	Pjotr Prins Lab	https://doi.org/10.1093/bioinformatics/btv098
LDC (v1.20.1)	N/A	https://github.com/ldc-developers/ldc
DMD (v2.090.1)	D Language Foundation	https://dlang.org/
LLVM (v9.0.1)	LLVM Developer Group	https://llvm.org/
samtools (v1.10)	Richard Durbin Lab	https://doi.org/10.1093/bioinformatics/btp352
htslib (v1.14)	Andrew Whitwham	https://doi.org/10.1093/gigascience/giab007
bedtools (v2.27.1)	Aaron R. Quinlan Lab	https://doi.org/10.1093/bioinformatics/btq033
deeptools (v3.5.1)	Thomas Manke Lab	https://doi.org/10.1093/nar/gku365
pyGenomeTracks (v3.8)	Thomas Manke Lab	https://doi.org/10.1093/bioinformatics/btaa692
STAR (v2.7.1a)	Alexander Dobin Lab	https://doi.org/10.1093/bioinformatics/bts635
STAR-Fusion (v2.7.1a)	Brian Haas	https://doi.org/10.1101/120295
RSEM (v1.3.1)	Colin N. Dewey Lab	https://doi.org/10.1186/1471-2105-12-323
MACS (v2.2.7.1)	X. Shirley Liu Lab	https://doi.org/10.1186/gb-2008-9-9-r137
bedGraph2Cluster (v5.3)	Michael S. Lawrence Lab	https://doi.org/10.1016/j.xpro.2022.101991
PanChIP (v3.0.10)	Michael S. Lawrence Lab	https://doi.org/10.1016/j.molcel.2022.07.014
HOMER (v4.11.1)	Christopher Benner Lab	https://doi.org/10.1016/j.molcel.2010.05.004
MEME Suite (v5.3.3)	Timothy L. Bailey Lab	https://doi.org/10.1093/nar/gkv416
Juicer Tools (v1.22.0)	Erez Lieberman Aiden Lab	https://doi.org/10.1016/j.cels.2016.07.002
JuiceBox (v1.11.08)	Erez Lieberman Aiden Lab	https://doi.org/10.1016/j.cels.2015.07.012

HiCCUPS (v1.22.0)	Erez Lieberman Aiden Lab	https://doi.org/10.1016/j.cell.2014.11.021
HiCCUPS Diff (v1.22.0)	Erez Lieberman Aiden Lab	https://doi.org/10.1016/j.cels.2016.07.002
APA (v1.22.0)	Erez Lieberman Aiden Lab	https://doi.org/10.1016/j.cell.2014.11.021
cooler (v0.9.2)	Leonid A. Mirny Lab	https://doi.org/10.1093/bioinformatics/btz540
coolpup.py (v1.0.0)	Open2C	https://doi.org/10.1093/bioinformatics/btaa073
cooltools (v0.5.2)	Open2C	https://doi.org/10.1101/2022.10.31.514564
hic2cool (v0.5.1)	4D Nucleome Network	https://github.com/4dn-dcic/hic2cool
HiCExplorer (v2.2.1.1)	Thomas Manke Lab	https://doi.org/10.1038/s41467-017-02525-w
Stripenn (v1.1.65.15)	Golnaz Vahedi Lab	https://doi.org/10.1038/s41467-022-29258-9
PGS (v0.0.1)	Frank Alber Lab	https://doi.org/10.1038/nprot.2018.008
FitHiChIP (v11.0)	Ferhat Ay Lab	https://github.com/ay-lab/FitHiChIP
ROSE (v0.1)	Richard A. Young Lab	https://doi.org/10.1016/j.cell.2013.03.035
RepEnrich (v2)	Steven W. Criscione	https://doi.org/10.1186/1471-2164-15-583
PyMOL (v2.5.2)	Schrödinger	https://pymol.org/
POV-Ray (v3.7.0.msvc10)	POV Team	https://www.povray.org/
ImageJ (v1.54d)	Wayne Resband	https://doi.org/10.1038/nmeth.2089

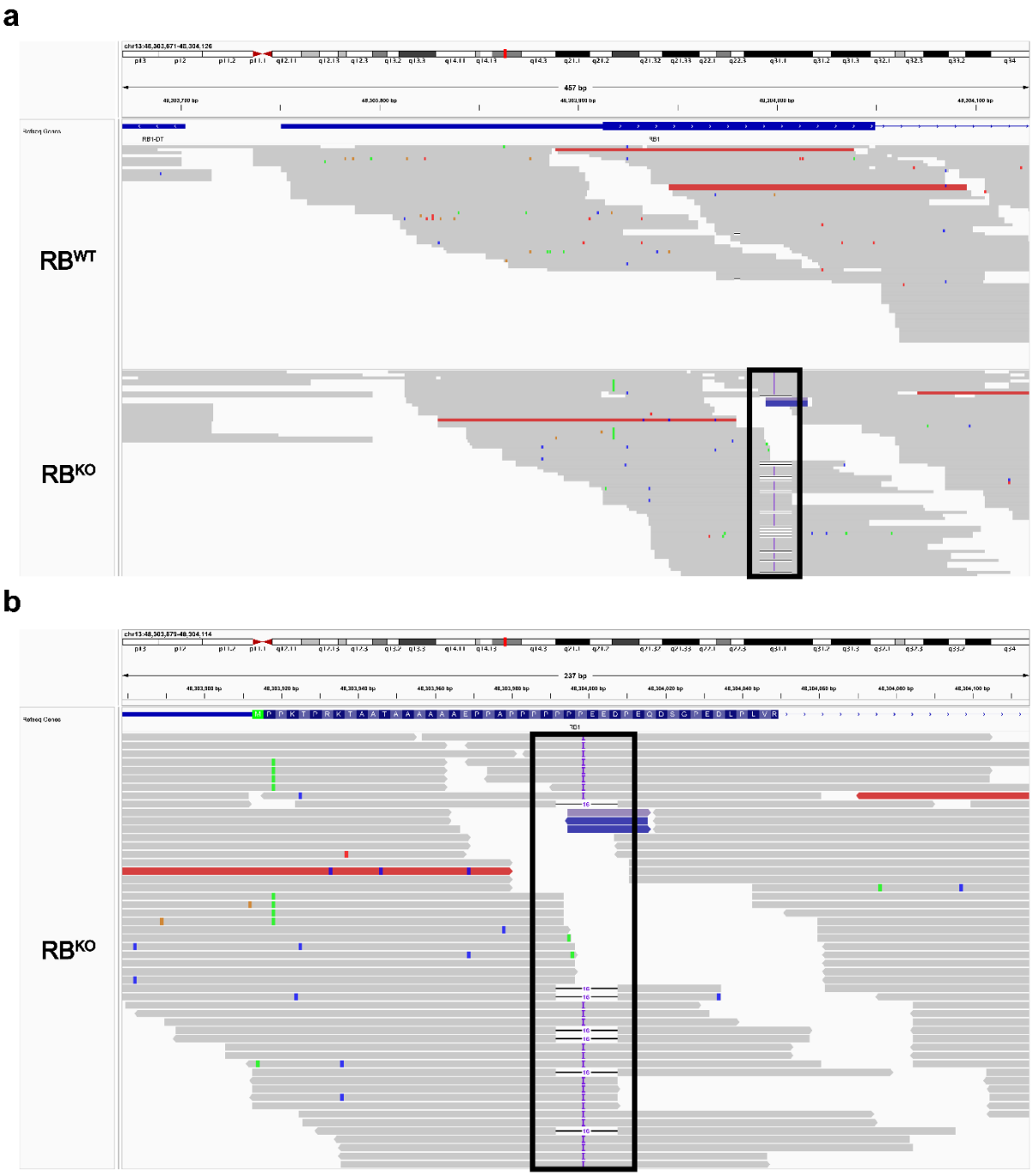

Supplementary Fig. 1. Validation of loss-of-function RB mutation in RB^{KO} clone.

(**a** and **b**) Integrative Genomic Viewer (IGV) screenshot of micrococcal nuclease sequencing (MNase-seq) reads from exon 1 of *RB1*. (a) Aligned reads from RB^{WT} and RB^{KO} clones reveal mutation specific to RB^{KO} at a locus targeted by the sgRNA. (b) Characterization of *RB1* mutation. RB^{KO} clone harbors a compound heterozygous mutation in *RB1*, with 1 bp insertion and 16 bp deletion in exon 1.

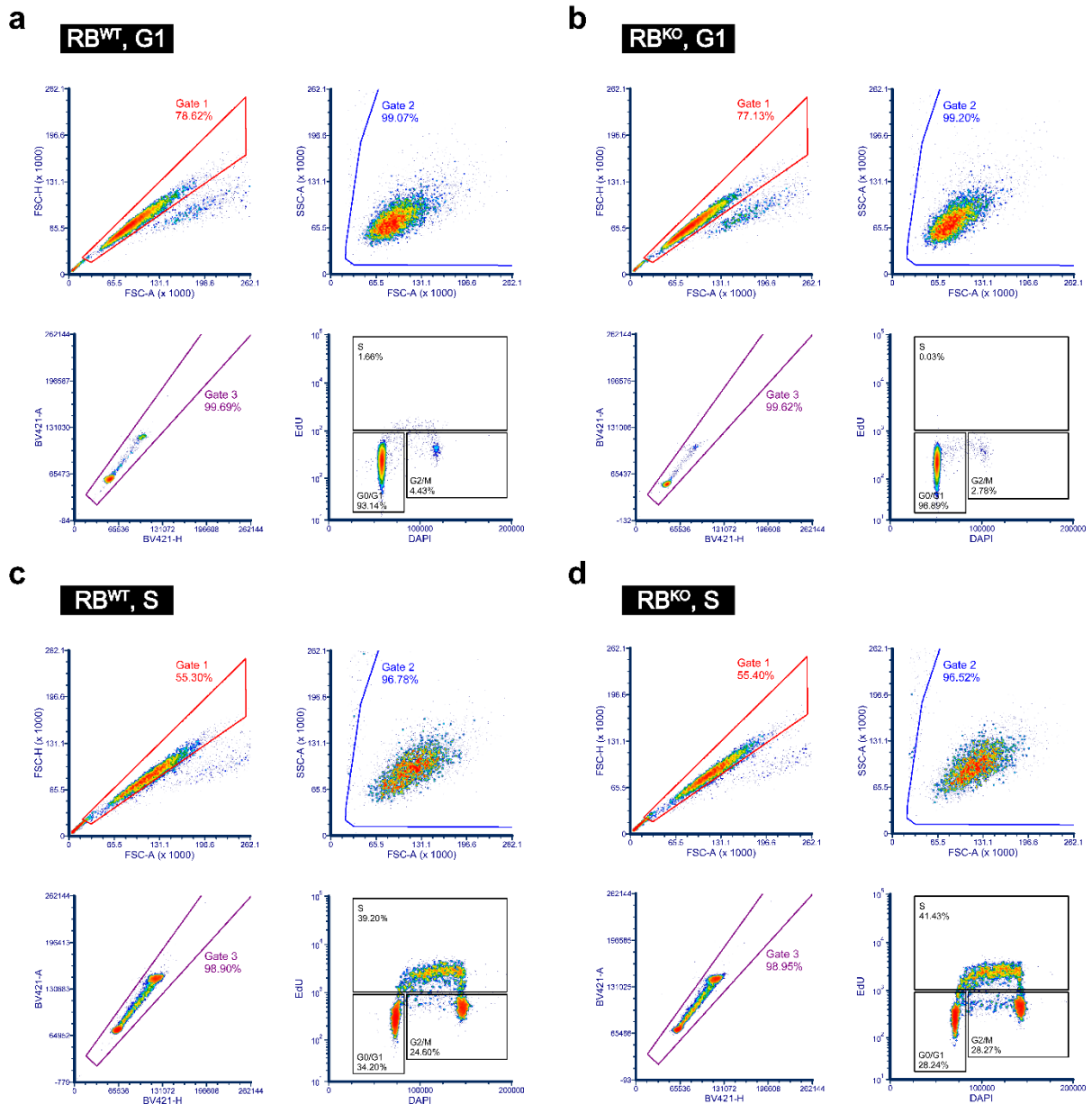

Supplementary Fig. 2. Contact inhibition reversibly arrests hTERT-RPE1 cells in G1 regardless of the presence of intact RB.

(**a** to **d**) Flow cytometry analysis of cell cycle using EdU and DAPI in hTERT-RPE1 cells. (a) RB^{WT} cells after 6 d of contact inhibition. (b) RB^{KO} cells after 6 d of contact inhibition. (c) RB^{WT} cells after 6 d of contact inhibition followed by trypsinization. (d) RB^{KO} cells after 6 d of contact inhibition followed by trypsinization. FSC-A, forward scatter area; FSC-H, forward scatter height; SSC-A, side scatter area; BV421-H, Brilliant Violet 421 channel height; BV421-A; Brilliant Violet 421 channel area; DAPI, 4′,6-diamidino-2-phenylindole; and EdU, 5-Ethynyl-2'-deoxyuridine.

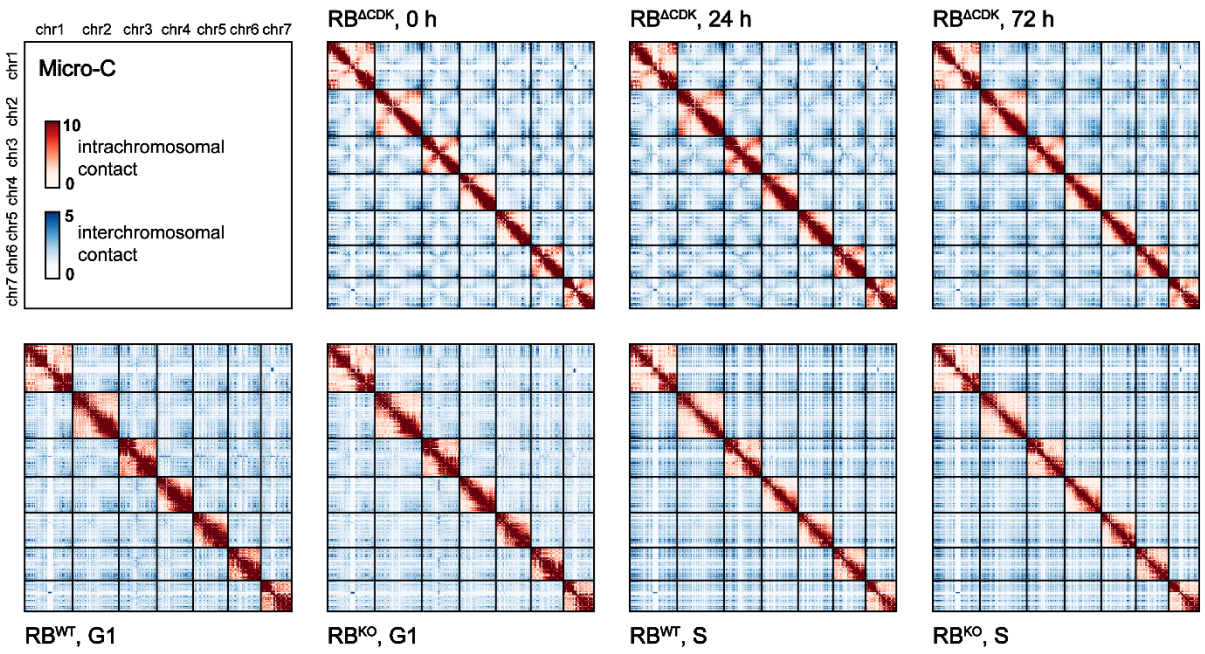

Supplementary Fig. 3. Chromosome conformation capture maps from Micro-C experiments.

Chromosome conformation capture maps visualized at 100 kb resolution. Chromatin contacts within and between chromosomes 1 to 7 are shown. Red, intrachromosomal contact; blue, interchromosomal contact.

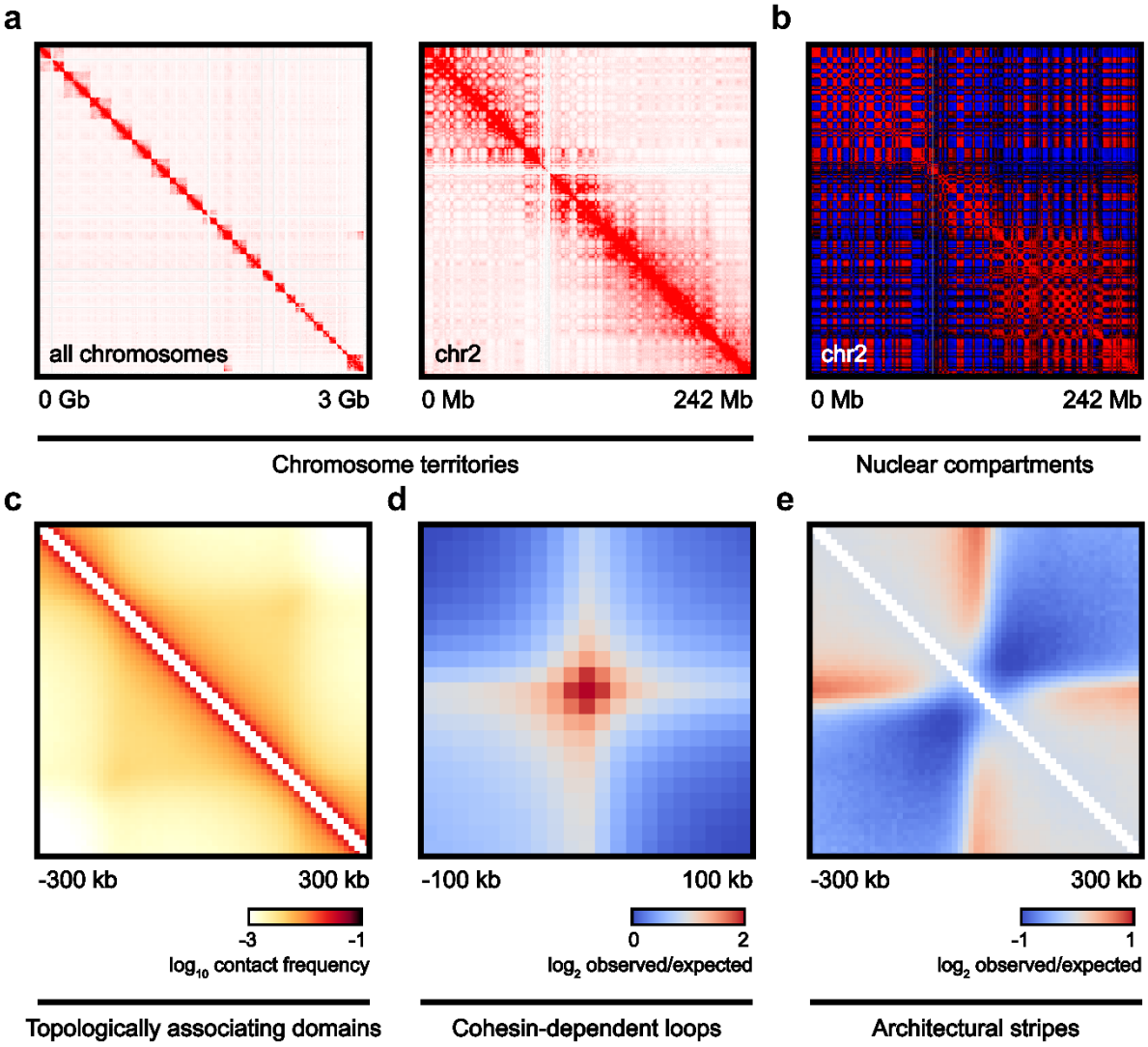

Supplementary Fig. 4. Micro-C recapitulates expected features of chromatin organization. (**a**) Chromosome conformation capture map for all chromosomes and chromosome 2. Intrachromosomal interactions indicate the chromosome territories. (**b**) Pearson correlation map for chromosome 2. Characteristic checkeraboard-like pattern is indicative of nuclear compartments. (**c**) $\log_{10}$ contact frequency map for topologically associating domains within 300 kb to 400 kb size range. (**d**) $\log_2$ observed/expected map for primary loops. (**e**) $\log_2$ observed/expected map for architectural stripes.

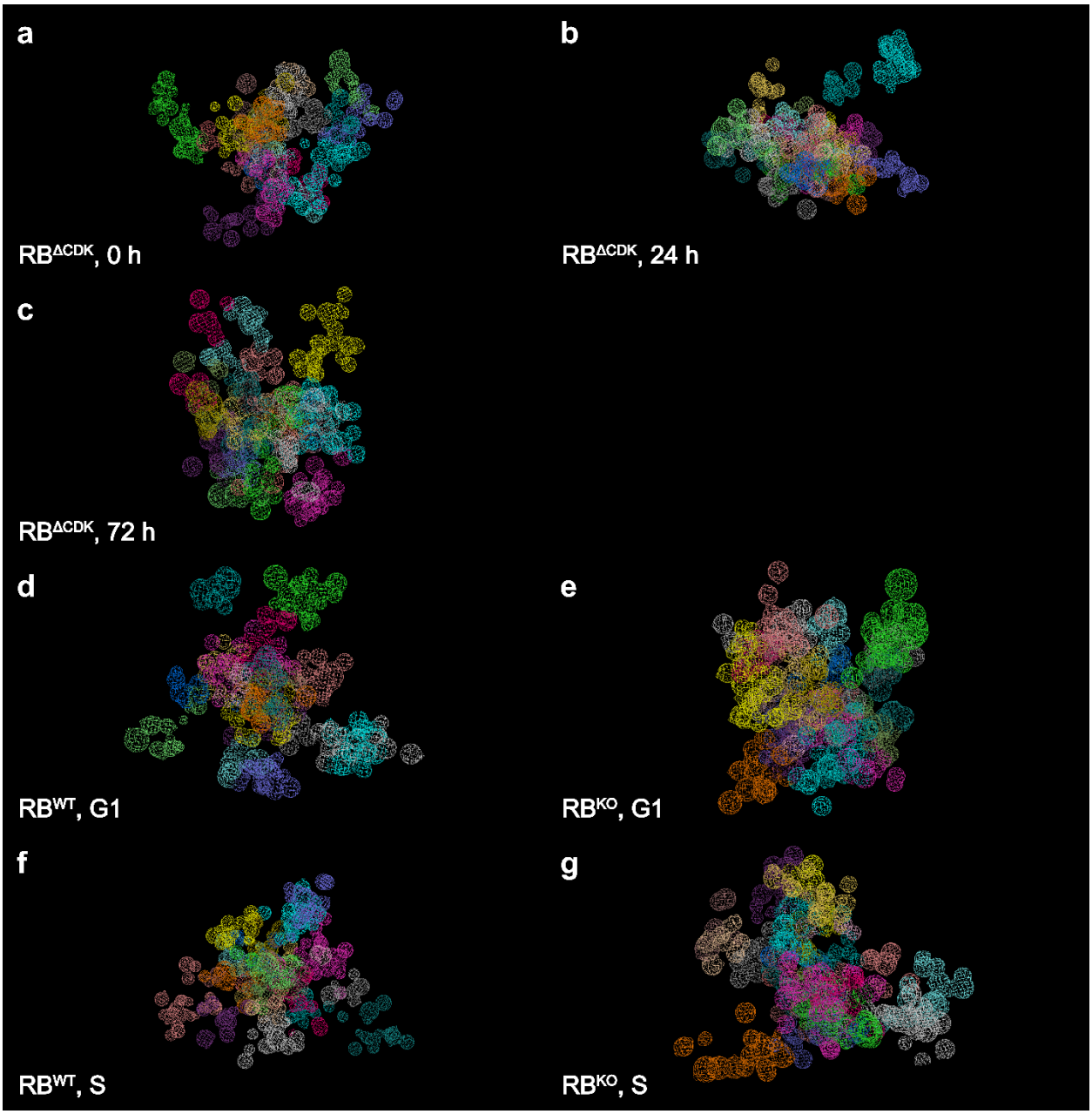

Supplementary Fig. 5. 3D reconstruction of nuclear structure via population-based algorithm.

(**a** to **g**) Average structure of each sample based on chromosome conformation capture. Each sphere indicates topologically associating domains. Color indicates individual chromosomes. (a) 0 h of $RB^{\Delta CDK}$ expression. (b) 24 h of $RB^{\Delta CDK}$ expression. (c) 72 h of $RB^{\Delta CDK}$ expression. (d) RB^{WT} cells synchronized in G1. (e) RB^{KO} cells synchronized in G1. (f) RB^{WT} cells released to S via trypsinization. (g) RB^{KO} cells released to S via trypsinization.

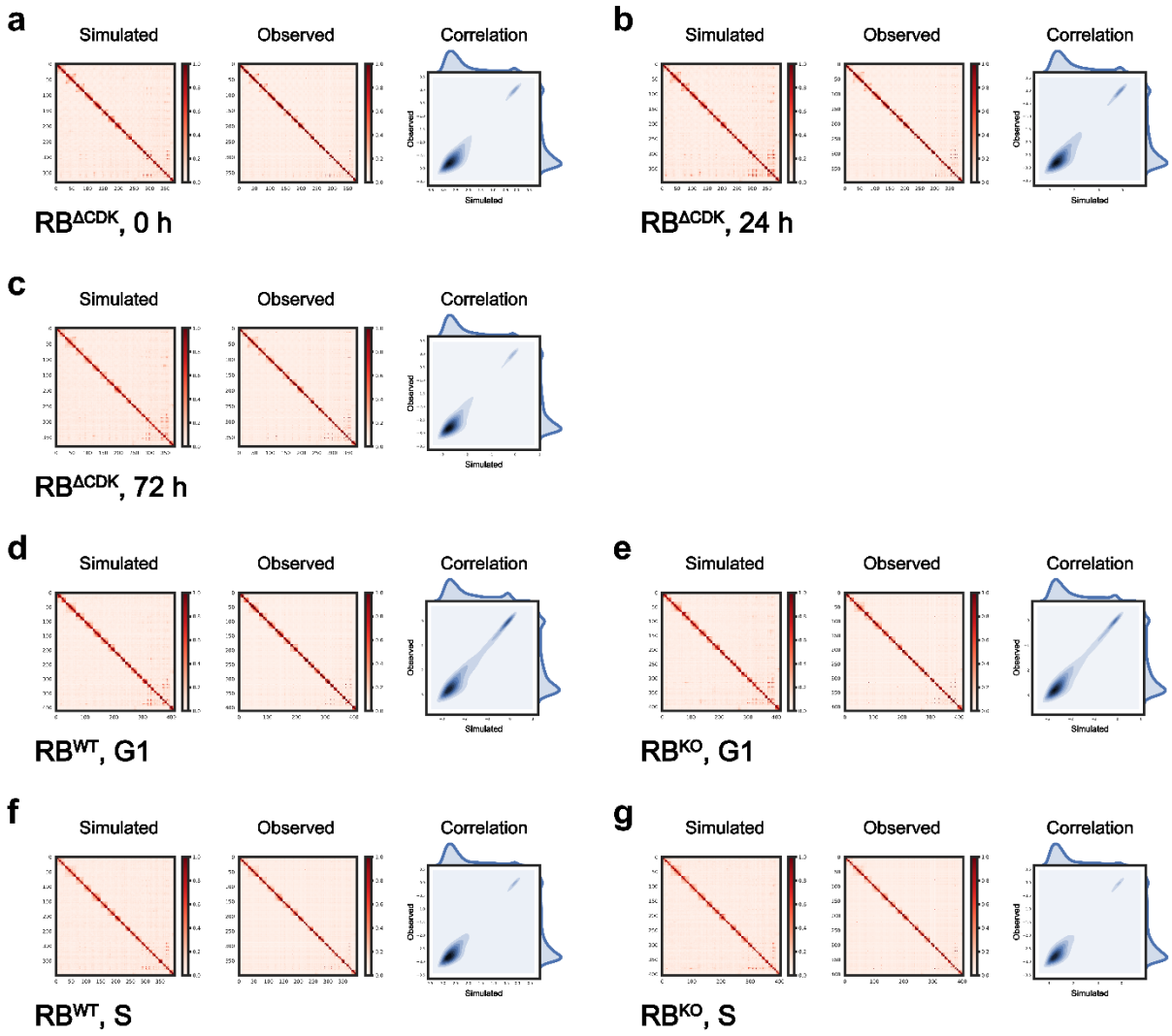

Supplementary Fig. 6. Validation of the 3D reconstruction of nuclear structure.

(**a** to **g**) Chromosome conformation capture maps generated from simulated (left) and observed (middle) data. The correlation between the simulated and the observed contacts are indicated in the right panel. (a) 0 h of $RB^{\Delta CDK}$ expression. (b) 24 h of $RB^{\Delta CDK}$ expression. (c) 72 h of $RB^{\Delta CDK}$ expression. (d) RB^{WT} cells synchronized in G1. (e) RB^{KO} cells synchronized in G1. (f) RB^{WT} cells released to S via trypsinization. (g) RB^{KO} cells released to S via trypsinization.

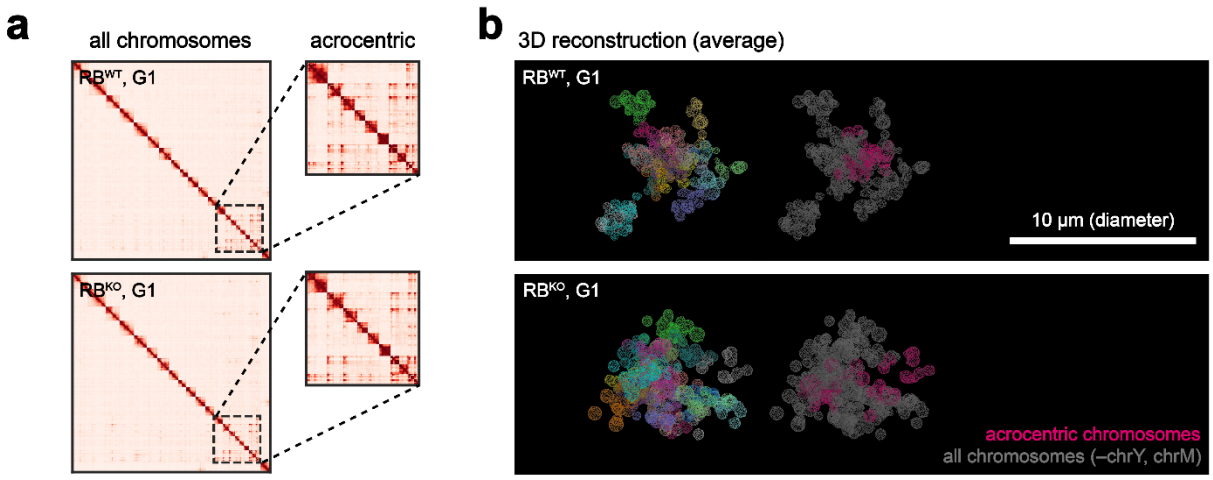

Supplementary Fig. 7. 3D reconstruction of nucleolar structure.

(**a**) Reconstructed chromosome conformation capture matrix visualized at 1 Mb resolution. Inset, interaction between acrocentric chromosomes containing the nucleolar organizer regions (NORs). (**b**) Reconstructed three-dimensional architecture of the nucleus. pink, acrocentric chromosomes; gray, all chromosomes. Scale bar, 10 μm.

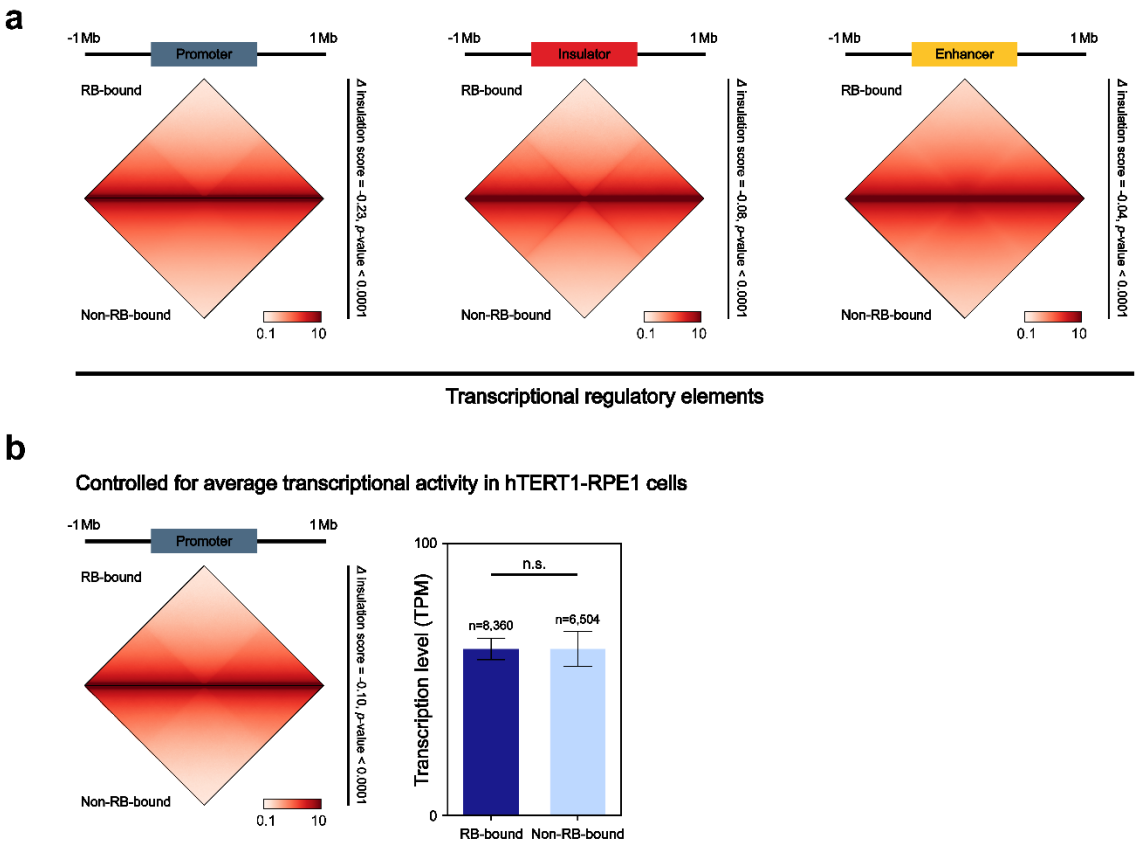

Supplementary Fig. 8. The effect of RB binding on chromatin insulation.

(**a**) Comparison of chromosome conformation capture map between RB-bound and non-RB-bound transcriptional regulatory elements. Left, promoters; middle, insulators; and right, enhancers. In all types of transcriptional regulatory elements, RB binding was associated with stronger chromatin insulation. (**b**) Comparison of chromosome conformation capture map between RB-bound promoters and non-RB-bound promoters controlled for average transcription level. Left, RB-bound promoters show stronger chromatin insulation compared to non-RB-bound promoters even after being controlled for the transcription level. Right, comparison of transcription level. Error bar, standard error. **p*-value < 0.05, ***p*-value < 0.01, and ****p*-value < 0.001.

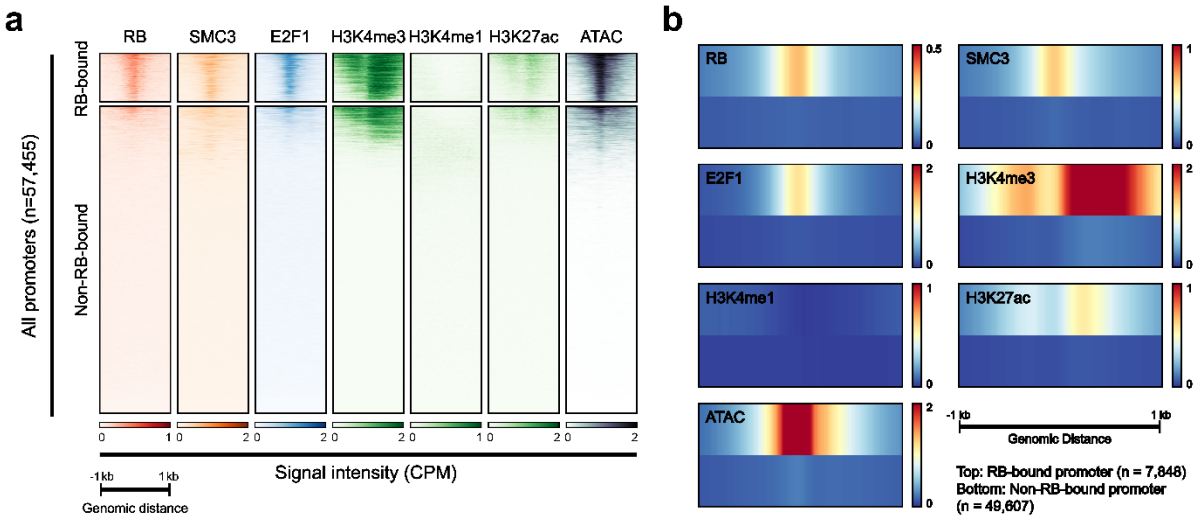

Supplementary Fig. 9. Comparison of RB-bound promoters and non-RB-bound promoters. (**a**) Heatmap showing average signal intensities for ChIP-seq experiments (RB, SMC3, E2F1, H3K4me3, H3K4me1, and H3K27ac) and ATAC-seq experiment. (**b**) Aggregate signals. Regions that are within 1 kb of the transcriptional start site are shown.

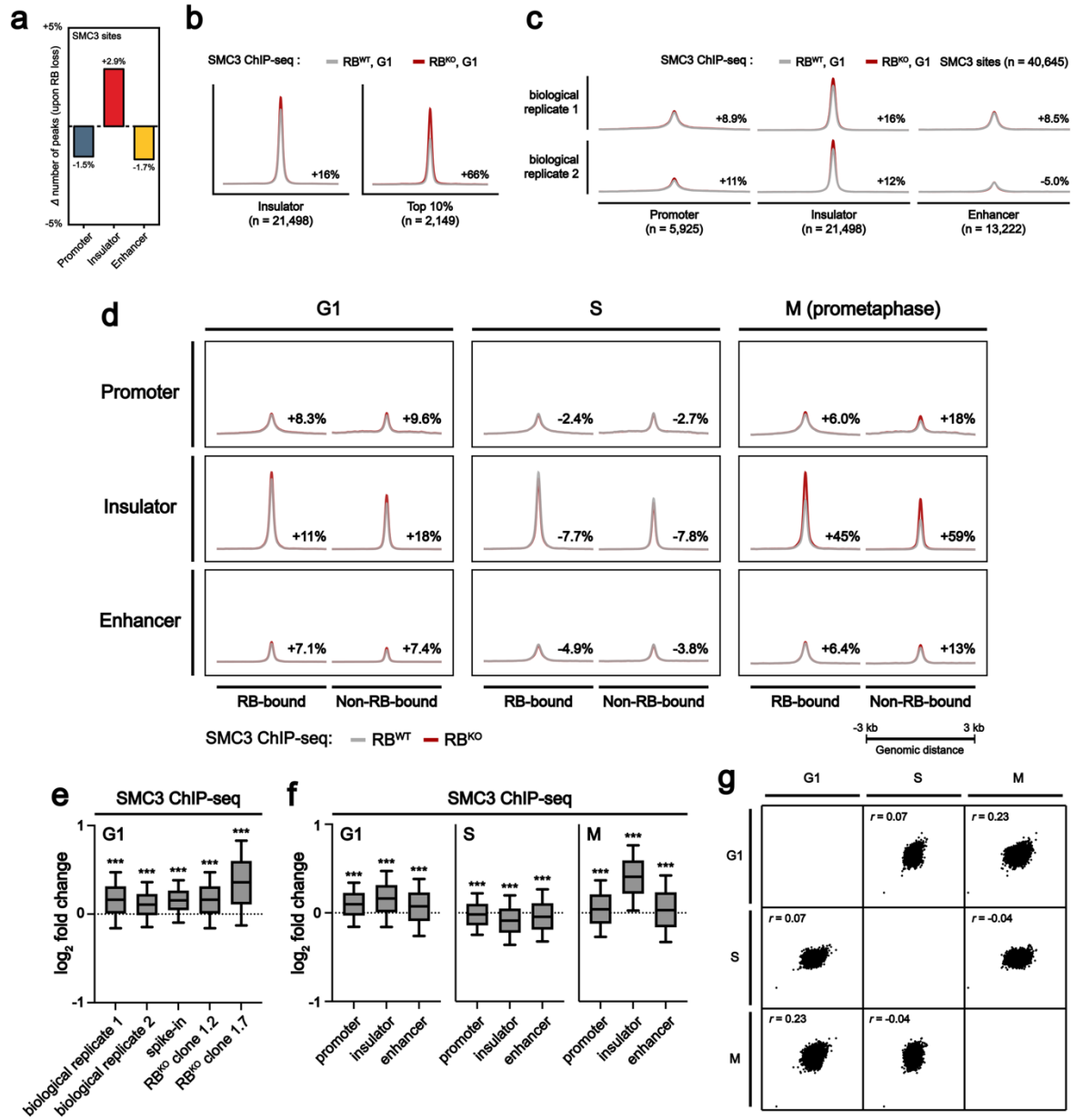

Supplementary Fig. 10. Characterization of SMC3 deregulation upon RB loss.

(**a**) Change in the number of SMC3 ChIP-seq peaks upon RB loss. We observed specific increase in the number of SMC3-bound insulator peaks. (**b**) SMC3 deregulation primarily occurs at weaker SMC3 sites. Regions that were within top 10% in SMC3 fold change exhibited an average 66% increase in SMC3 signal and had lower SMC3 signal compared to the average. (**c**) Biological replicate experiments confirm the change in SMC3 signal. (**d**) Change in SMC3 ChIP-seq signal at RB-bound and non-RB-bound SMC3 peaks. (**e** and **f**) Box plot of log2 fold change of SMC3 ChIP-seq signals at SMC3 peaks upon RB loss across experiments. SMC3 ChIP-seq signals at insulators in G1 phase (e) and across *cis*-regulatory elements in G1, S, and

prometaphase (f) are shown. The data confirms that the observed increase in SMC3 ChIP-seq signal at insulators in G1 and prometaphase cells occurs genome-wide and is not driven by outliers. One-sample Student's *t*-test was utilized to assess statistical significance and Bonferroni correction was utilized for multiple hypotheses correction. (**g**) Scatter plot of log2 fold change of SMC3 signals between different phases of the cell cycle. Pearson's correlation coefficient is shown on the upper left. We show that G1 and prometaphase cells are positively correlated, while S phase cells have little to no correlation with both. **p*-value < 0.05, ***p*-value < 0.01, and ****p*-value < 0.001.

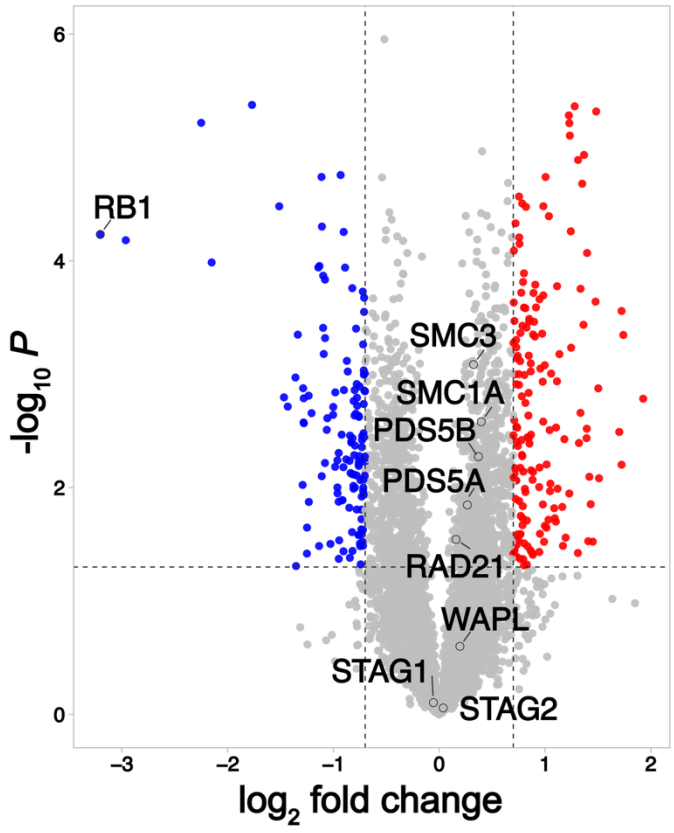

Supplementary Fig. 11. Proteomic analysis shows no difference in cohesin complex protein levels between RB^{WT} and RB^{KO} hTERT-RPE1 cells arrested in G1-phase.
Volcano plot showing differential protein expression between RB^{WT} and RB^{KO} hTERT-RPE1 cells arrested in G1 phase by 6 days of contact inhibition before quantitative mass spectrometry analysis. The x-axis represents the $\log_2$ fold change (FC) in protein abundance between RB^{WT} and RB^{KO} cells, with positive values indicating higher levels in RB^{KO} cells and negative values indicating higher levels in RB^{WT} cells. The y-axis represents $-\log_{10}P$, reflecting statistical significance. Proteins above the horizontal dashed line ($P < 0.05$) are considered statistically significant. Vertical dashed lines mark $\log_2$FC thresholds of > 0.7 or < -0.7 used to define substantial expression changes. Red and blue dots represent proteins significantly more abundant in RB^{KO} and RB^{WT} cells, respectively; gray dots indicate proteins without significant differential expression. As expected, RB protein levels were significantly reduced in the RB^{KO} cells. The levels of the cohesin complex components SMC3, SMC1A, PDS5B, PDS5A, RAD21, STAG1, STAG2 and the cohesin release factor WAPL were comparable between RB^{WT} and RB^{KO} cells. Data represent four independent biological replicates.

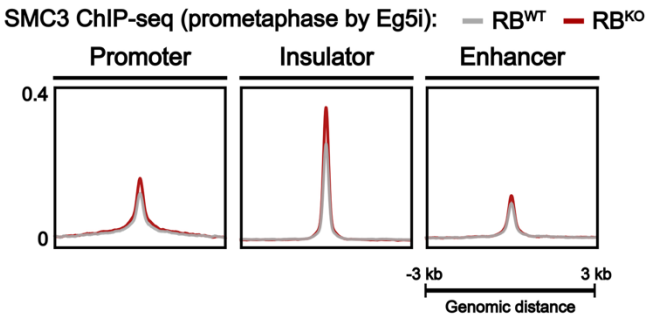

Supplementary Fig. 12. Prometaphase arrest by Eg5 inhibition reveals SMC3 redistribution toward insulators upon RB loss.
Aggregate plots showing the average SMC3 ChIP-seq signal across indicated genomic features (Promoter, Insulator, Enhancer) in prometaphase arrested RB^{WT} (grey) and RB^{KO} (red) hTERT-RPE1 cells. Prometaphase arrest was performed by Eg5 inhibition. The x-axis represents genomic distance centered at the respective feature and the y-axis represents normalized ChIP-seq signal. The plots reveal a distinct increase in SMC3 enrichment at insulator regions upon RB loss, similar to the results obtained by nocodazole-induced prometaphase arrest (Fig. 3b).

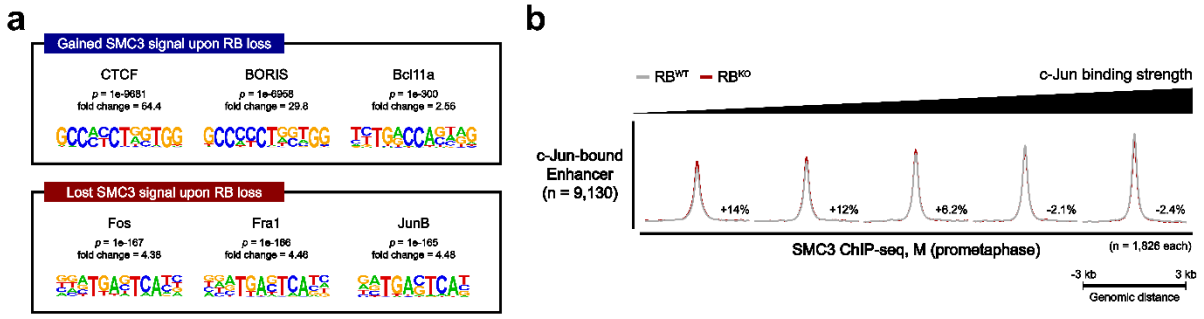

Supplementary Fig. 13. DNA motif analysis of regions that gained and lost SMC3 signal upon RB loss.

(**a**) Top three hits from the HOMER motif analysis. (**b**) Change in SMC3 ChIP-seq signal in c-Jun-bound enhancers. While strongest c-Jun-bound regions showed slight reductions, we observed overall gain of SMC3 signal upon RB loss, indicating that AP-1-bound enhancers are not the primary source of SMC3 during deregulation.

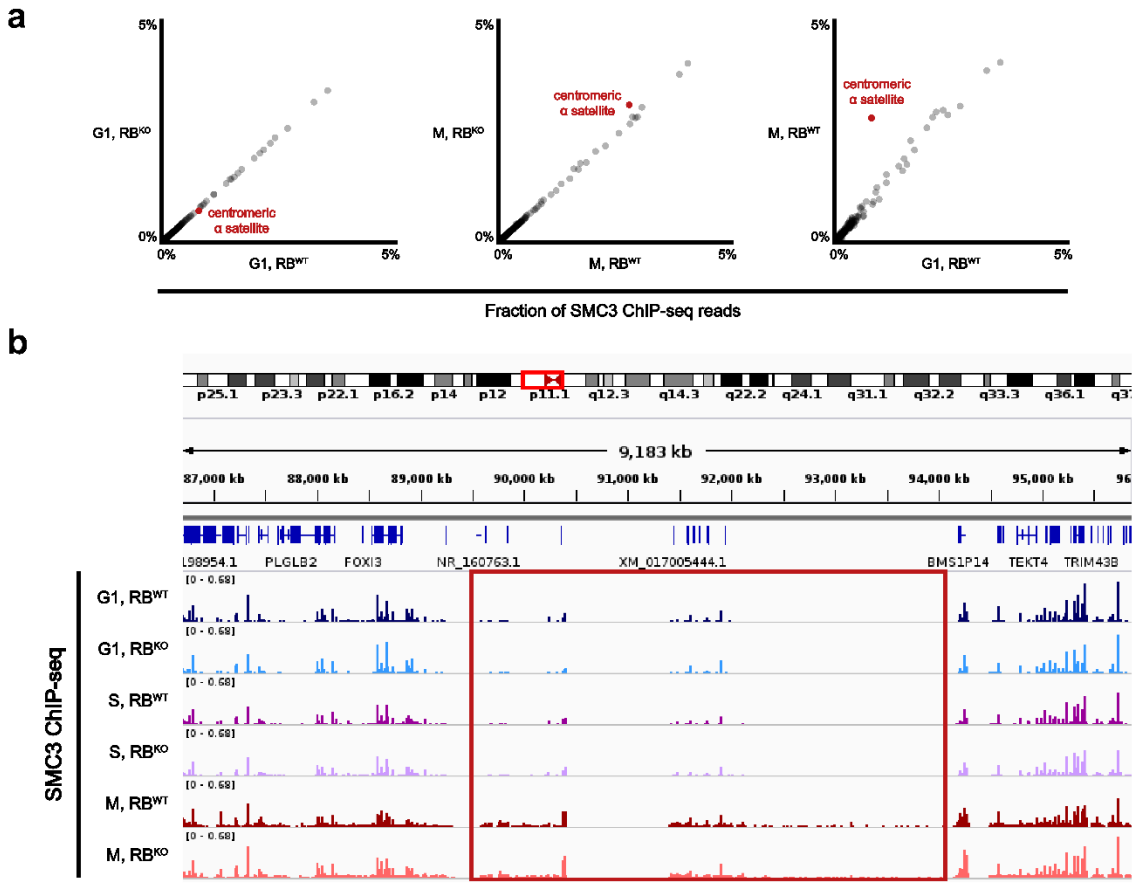

Supplementary Fig. 14. Change in SMC3 signal at DNA repeats.

(**a**) Scatter plot of SMC3 signal across 1,267 families of DNA repeats. Each axis indicates the fraction of reads aligned to each family. We observed a specific change in centromeric *α*-satellites. However, upon RB loss in the mitotic phase, we observed slightly increased number of reads aligned to centromeric *α*-satellites, indicating that these are not the primary source of SMC3 deregulation. Notably, we observed dramatic increase in SMC3 signal upon mitotic entry at centromeric *α*-satellites. (**b**) IGV screenshot of SMC3 signals at pericentromeric regions. We observed a dramatic increase in SMC3 signal upon mitotic entry.

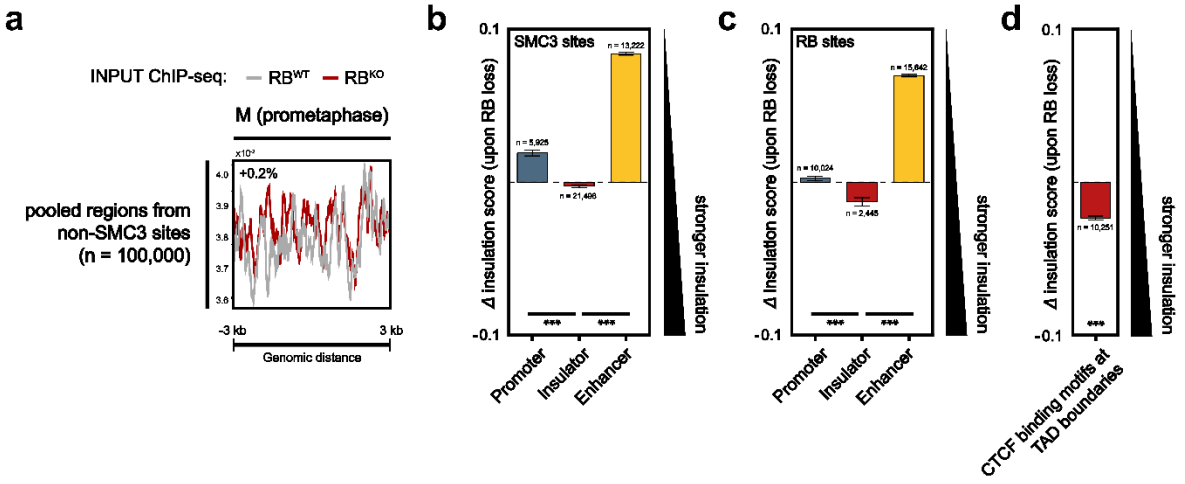

Supplementary Fig. 15. Characterization of SMC3 deregulation and insulation change.

(**a**) Comparison of DNA Input ChIP-seq signals at pooled regions from non-SMC3 sites performed as a negative control. We observed no differences between the two experiments. (**b** to **d**) Change in insulation score upon RB loss measured from chromosome conformation capture. (b) Insulation score at SMC3 sites. (c) Insulation score at RB sites. (d) Insulation score at TAD boundaries centered at CTCF binding motifs.

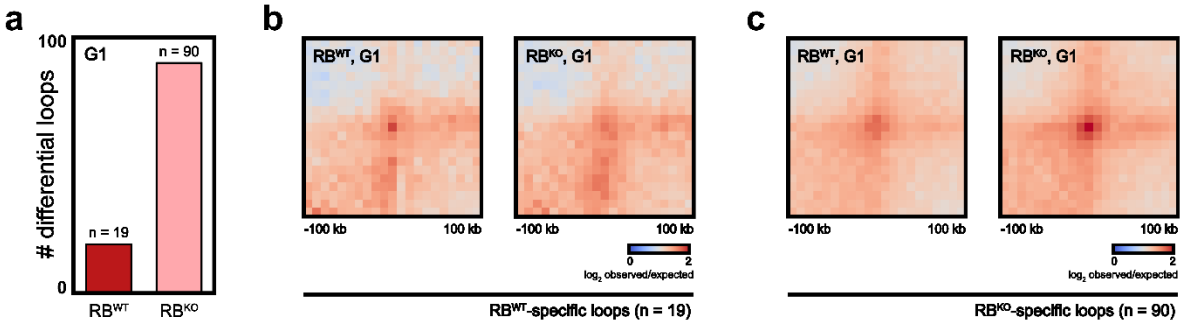

Supplementary Fig. 16. Differential loop analysis between G1-synchronized RB^{WT} and RB^{KO} cells.

(**a**) The number of differential loops specific to each sample identified by HiCCUPS Diff. (**b** and **c**) Comparison of aggregate peaks between RB^{WT} and RB^{KO} samples. (b) Chromatin loops specific to RB^{WT} cells. (c) Chromatin loops specific to RB^{KO} cells.

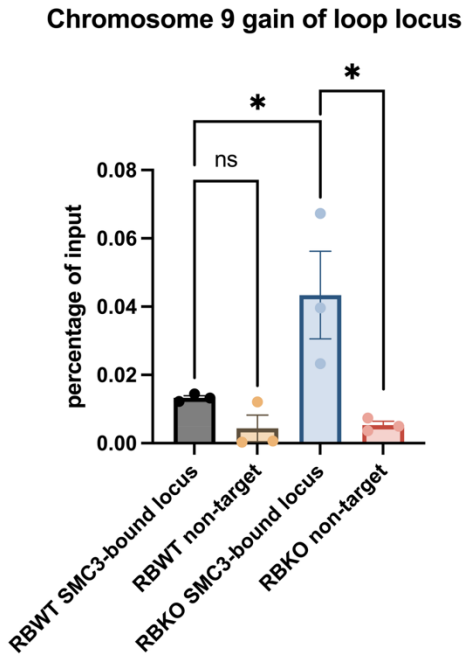

Supplementary Fig. 17. ChIP-qPCR confirms differential SMC3 recruitment to the locus of chromatin loop gain at chromosome 9.
ChIP-qPCR experiment was performed at the site of differential chromatin loop formation in chromosome 9 identified in Fig. 3i. Primer pairs targeting the SMC3-bound locus were used to probe SMC3 binding at the locus, while primer pairs targeting the non-targeting locus 500 bp away from the SMC3-bound locus were utilized as the negative control. ChIP-qPCR signal for SMC3 increased upon RB loss, corroborating our ChIP-seq and Micro-C results (not shown here). Statistical significance was determined by one-way ANOVA, $p<0.05$*.

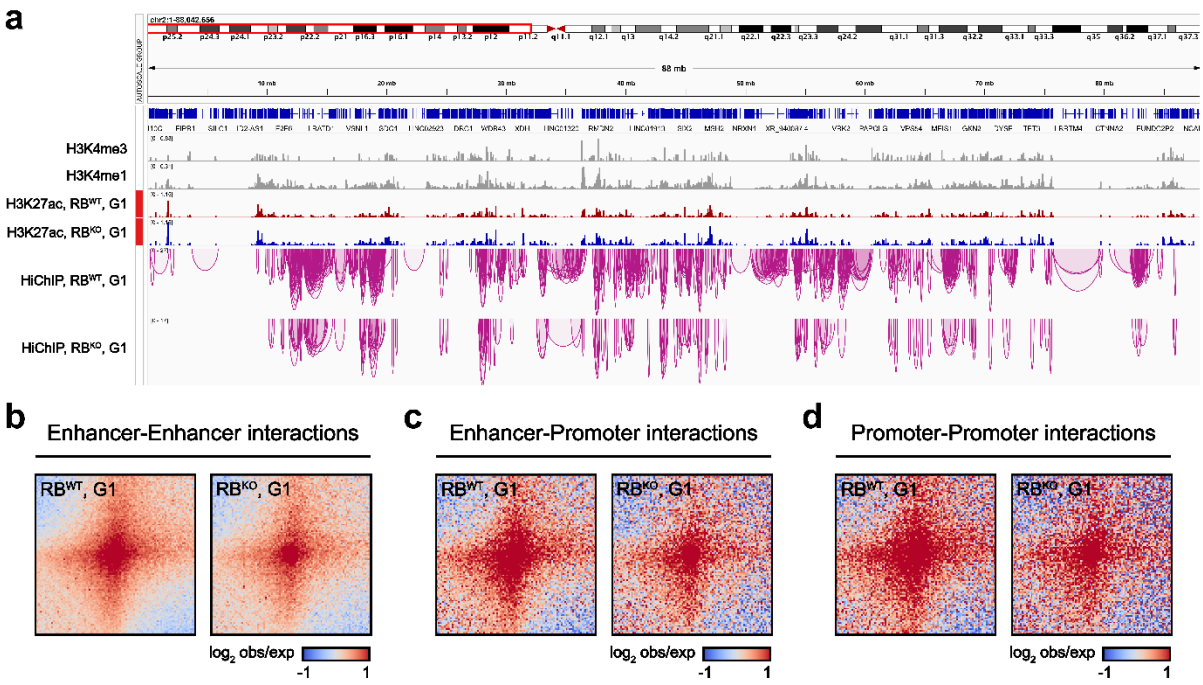

Supplementary Fig. 18. Change in H3K27ac HiChIP contacts upon RB loss.

(**a**) IGV screenshot of HiChIP peaks upon RB loss. ChIP-seq tracks for H3K4me3, H3K4me1, and H3K27ac modifications are also shown. Notably, we observed that the change in the HiChIP peaks did not correlate with the change in the H3K27ac ChIP-seq signal. (**b** to **d**) Aggregate HiChIP peaks are shown for each category. (b) Enhancer-enhancer interactions (n = 4,439). (c) Enhancer-promoter interactions (n = 637). (d) Promoter-promoter interactions (n = 254).

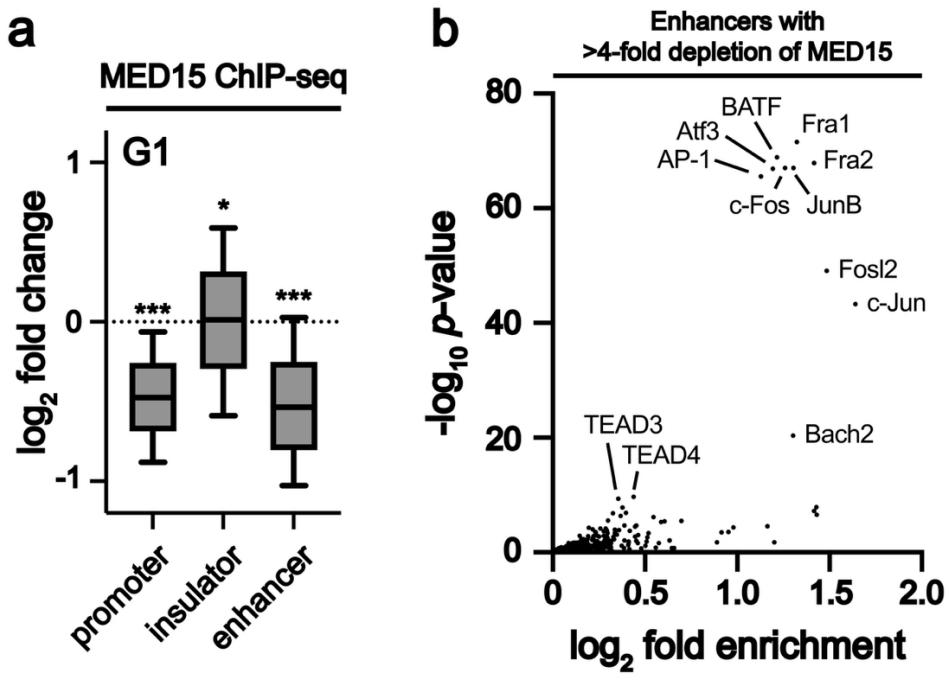

Supplementary Fig. 19. RB loss leads to MED15 depletion at promoters and enhancers.

(**a**) Box plot of log2 fold change of MED15 ChIP-seq signals across *cis*-regulatory elements in hTERT-RPE1 cells. RB loss led to statistically significant depletion of MED15 at promoters and enhancers. One-sample Student's *t*-test was utilized to assess statistical significance and Bonferroni correction was utilized for multiple hypotheses correction. (**b**) Motif enrichment analysis of enhancers with more than 4-fold depletion of MED15 revealed enrichment of DNA bindings motifs for AP-1 and TEAD transcription factors. **p*-value < 0.05, ***p*-value < 0.01, and ****p*-value < 0.001.

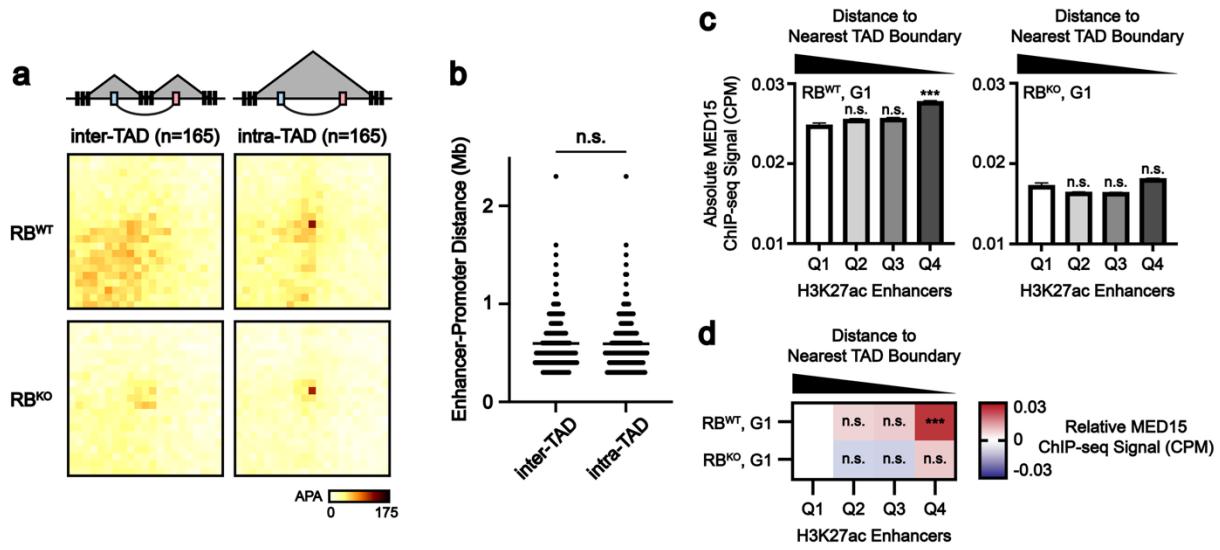

Supplementary Fig. 20. RB-dependent effects on enhancer-promoter interaction.

(**a**) Aggregate Peak Analyses (APA) of H3K27ac HiChIP experiment for inter-TAD and intra-TAD enhancer-promoter interactions controlled for enhancer-promoter distance (n=165 each). Intra-TAD enhancer-promoter interactions were stronger and more well-defined, while inter-TAD enhancer-promoter interactions were weaker and less distinct in both RB^{WT} and RB^{KO} hTERT-RPE1 cells. While both intra- and inter-TAD interactions become weaker upon RB loss, RB-dependent effect was more pronounced when enhancer-promoter interactions cross a TAD boundary. (**b**) Comparison of enhancer-promoter distance between inter-TAD and intra-TAD enhancer-promoter interaction sets controlled for enhancer-promoter distance. The distribution of enhancer-promoter distance was highly similar in these sets (*p*-value=1.0, two-tailed Student's *t*-test). (**c**) Absolute MED15 ChIP-seq signals averaged across enhancers marked with H3K27ac modifications. Enhancers were categorized into quartiles based on their distance to nearest TAD boundary. Average MED15 ChIP-seq signal is presented as counts per million (CPM). Left panel presents MED15 ChIP-seq signals in RB^{WT} hTERT-RPE1 cells arrested in G1 phase, while right panel presents MED15 ChIP-seq signals in RB^{KO} hTERT-RPE1 cells arrested in G1 phase. TAD boundary exerted a distance-dependent effect on MED15 recruitment to enhancers in RB^{WT} hTERT-RPE1 cells. This distance-dependent effect was abolished in RB^{KO} hTERT-RPE1 cells. (**d**) Heatmap of relative MED15 ChIP-seq signal compared to the enhancer quartile that is most distal from TAD boundaries. Notably, the TAD boundary-dependent effects on MED15 recruitment to enhancers did not fully explain the difference between RB^{WT} and RB^{KO} hTERT-RPE1 cells, suggesting that there may be effects of RB loss that are independent of its role in regulating insulation at TAD boundaries. Two-tailed Student's *t*-test was performed to assess statistical significance, and Bonferroni correct was performed for multiple hypotheses correction. **p*-value < 0.05, ***p*-value < 0.01, and ****p*-value < 0.001.

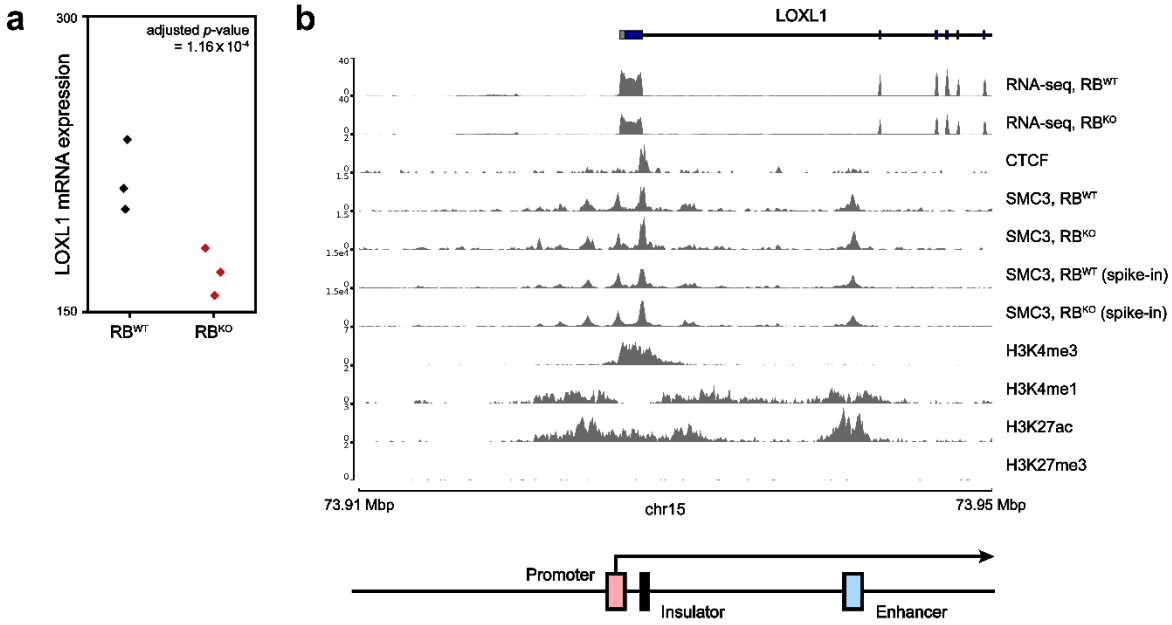

Supplementary Fig. 21. Individual example of cohesin gain gene set.

(**a**) Individual example of decrease in mRNA expression upon RB loss in the cohesin gain gene set. *LOXL1*, lysyl oxidase-like 1. (**b**) RNA-seq and ChIP-seq tracks for chromatin regions encompassing *LOXL1* transcriptional regulatory elements. **p*-value < 0.05, ***p*-value < 0.01, and ****p*-value < 0.001.

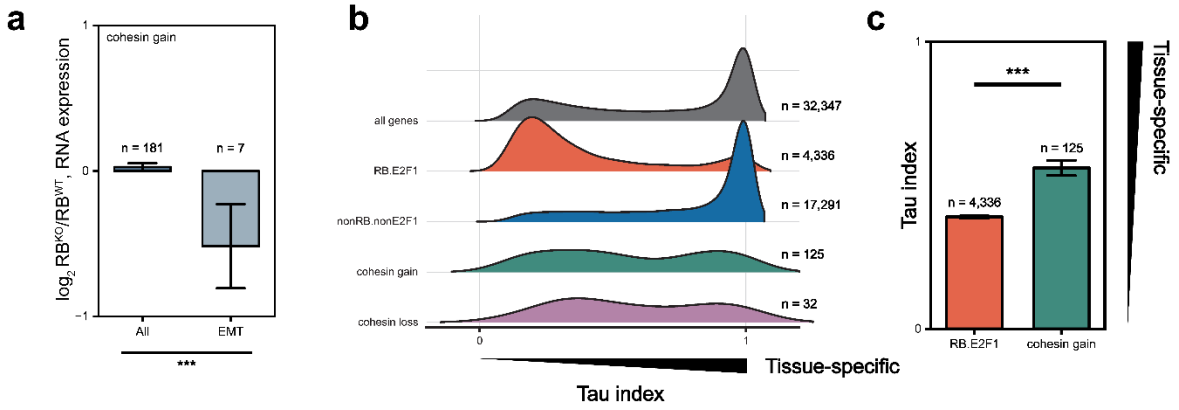

Supplementary Fig. 22. Further characterization of the cohesin gain gene set.

(**a**) Genes belonging to both the cohesin gain gene set and the epithelial-mesenchymal transition gene set show downregulation upon RB loss. EMT, epithelial-mesenchymal transition. (**b**) Comparison of tau tissue-specificity index between different gene sets. Compared to promoters that are bound by both RB and E2F, those that are not bound by RB and E2F, including both the cohesin gain and cohesin loss gene sets, are expressed in a more tissue-specific manner in the GTEx database. (**c**) Comparison of the tau tissue-specificity index between genes with promoters that are bound by both RB and E2F and the cohesin gain gene set. Error bar, standard error. **p*-value < 0.05, ***p*-value < 0.01, and ****p*-value < 0.001.

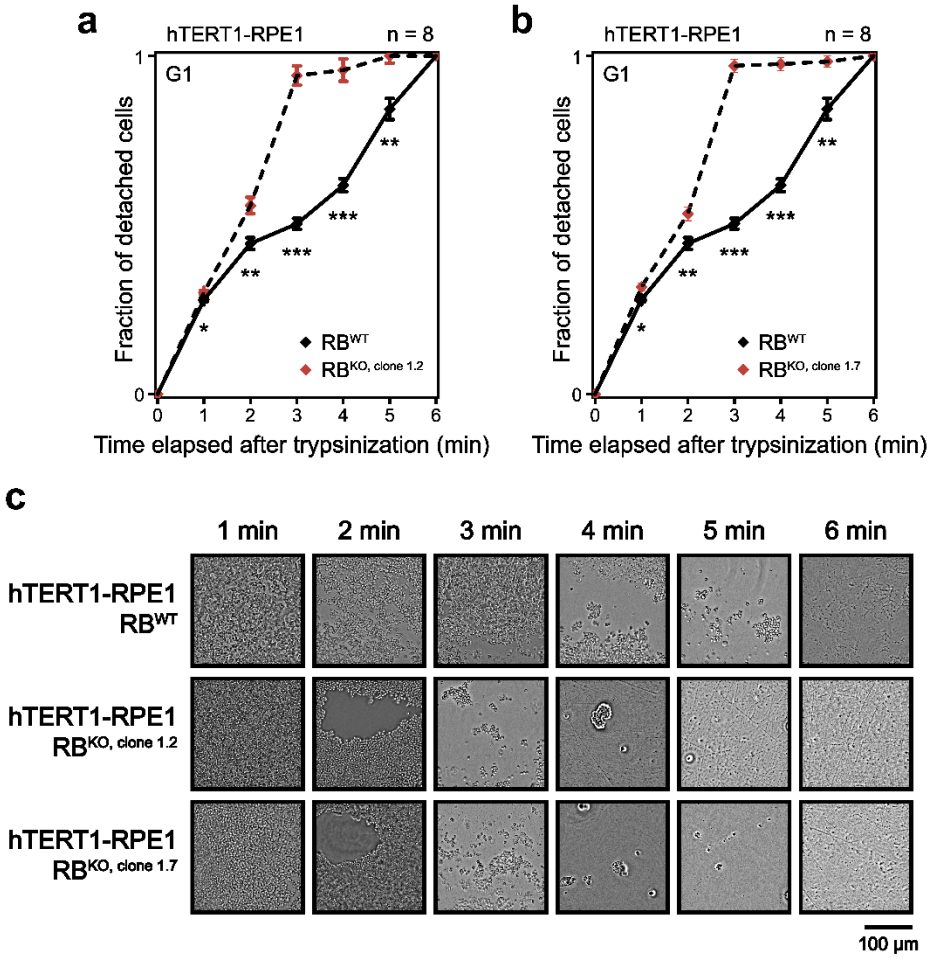

Supplementary Fig. 23. Comparison of cellular detachment rate upon trypsinization between RB-positive and RB-negative cells.

(**a** and **b**) Fraction of detached cells following trypsinization in cells synchronized in G1. In all experiments, RB-negative cells detached significantly faster compared to RB-positive cells. (a) Comparison between RB^{WT} and clone 1.2 of RB^{KO} in hTERT-RPE1 cells. (b) Comparison between RB^{WT} and clone 1.7 of RB^{KO} in hTERT-RPE1 cells. (**c**) Representative images of the trypsinization experiment for each timepoint. Error bar, standard error. Scale bar, 100 µm. **p*-value < 0.05, ***p*-value < 0.01, and ****p*-value < 0.001.

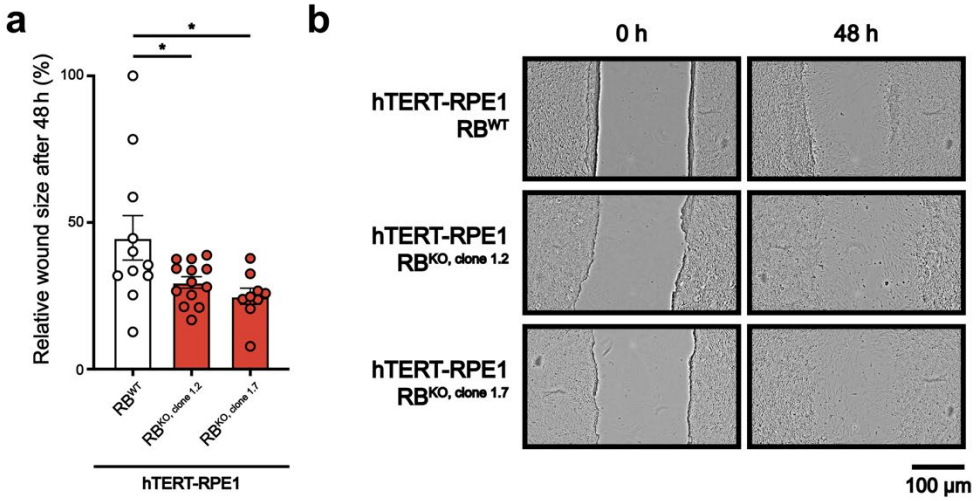

Supplementary Fig. 24. Comparison of wound healing rate between RB-positive and RB-negative cells.

(**a** and **b**) Wound healing assay in hTERT-RPE1 cells. (a) Comparison between RB^{WT} and different clones of RB^{KO} cells of the wound area upon 48 h of incubation as a percentage of the initial wound area. (b) Representative images of the wound healing experiment for each timepoint. Error bar, standard error. Scale bar, 100 µm. **p*-value < 0.05, ***p*-value < 0.01, and ****p*-value < 0.001.

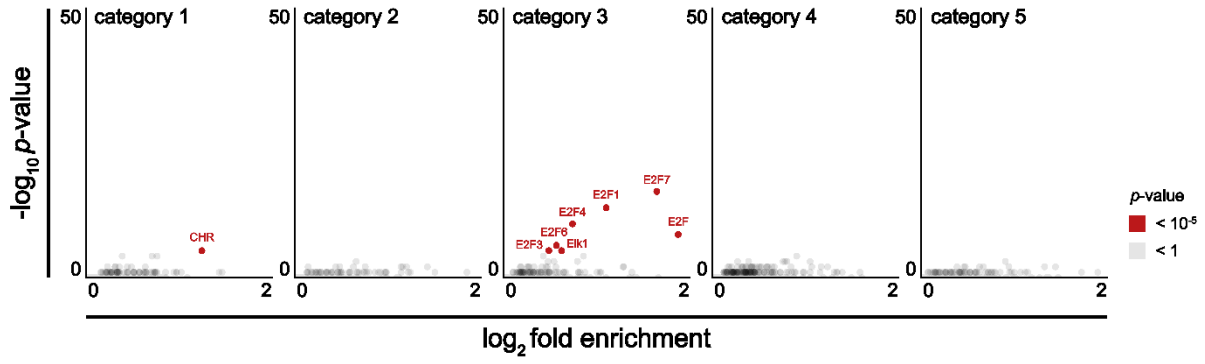

Supplementary Fig. 25. Volcano plot of DNA motif enrichment at RB-regulated promoters. HOMER motif analysis was performed on promoter regions for genes from each category. Motifs that showed *p*-value less than 10^{-5} are colored in red. Category 1 genes were enriched with CHR motifs, while category 3 genes were enriched with E2F motifs. Other categories exhibited generally weaker DNA motif enrichment.

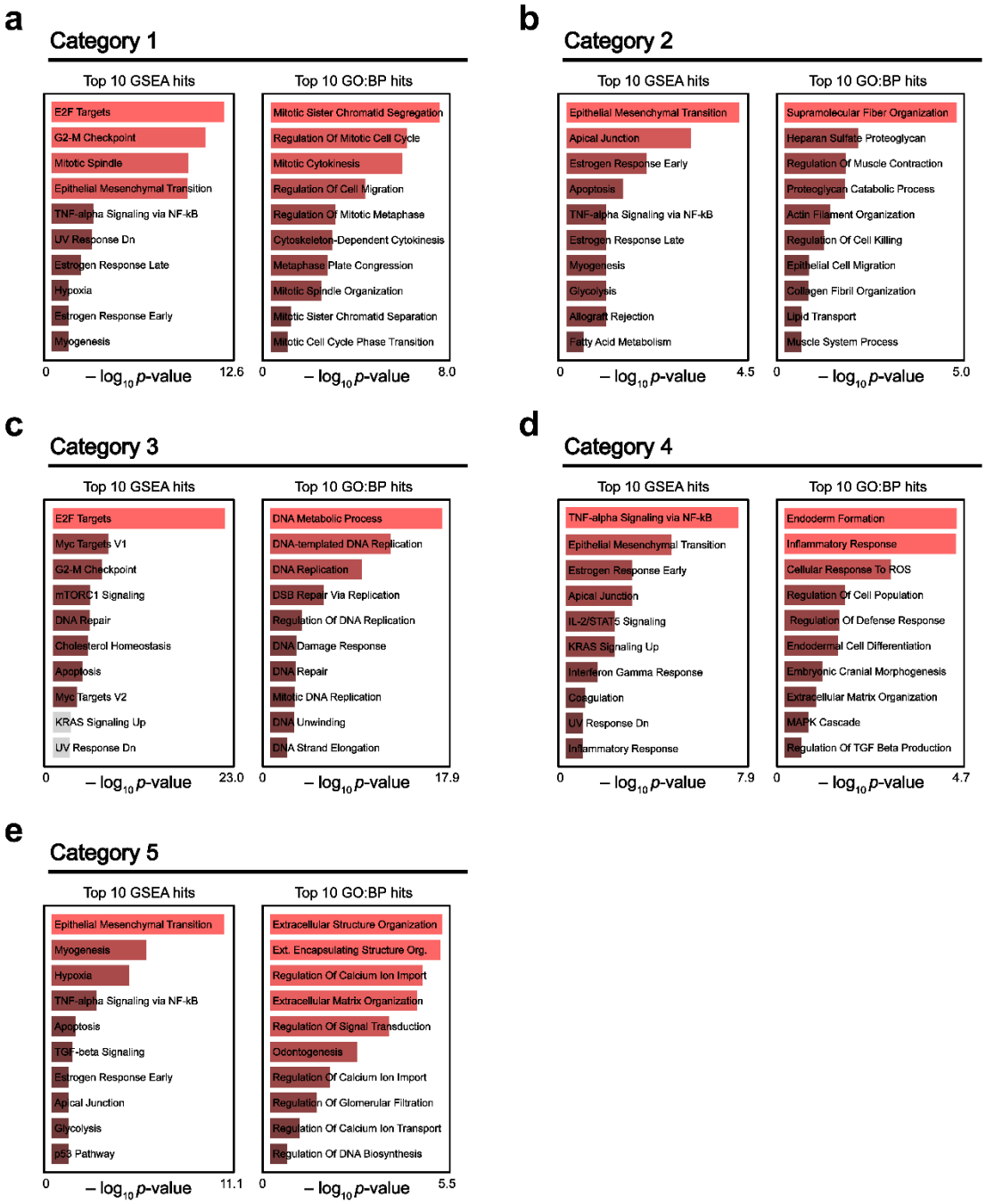

Supplementary Fig. 26. Gene set enrichment and gene ontology analyses results for each transcriptional regulation category identified from RNA-seq experiments.

(**a** to **e**) Top gene set enrichment and gene ontology hits and their statistical significance. Left, gene set enrichment analysis; and right, gene ontology analysis. GSEA, gene set enrichment analysis; GO, gene ontology; and BP, biological process.

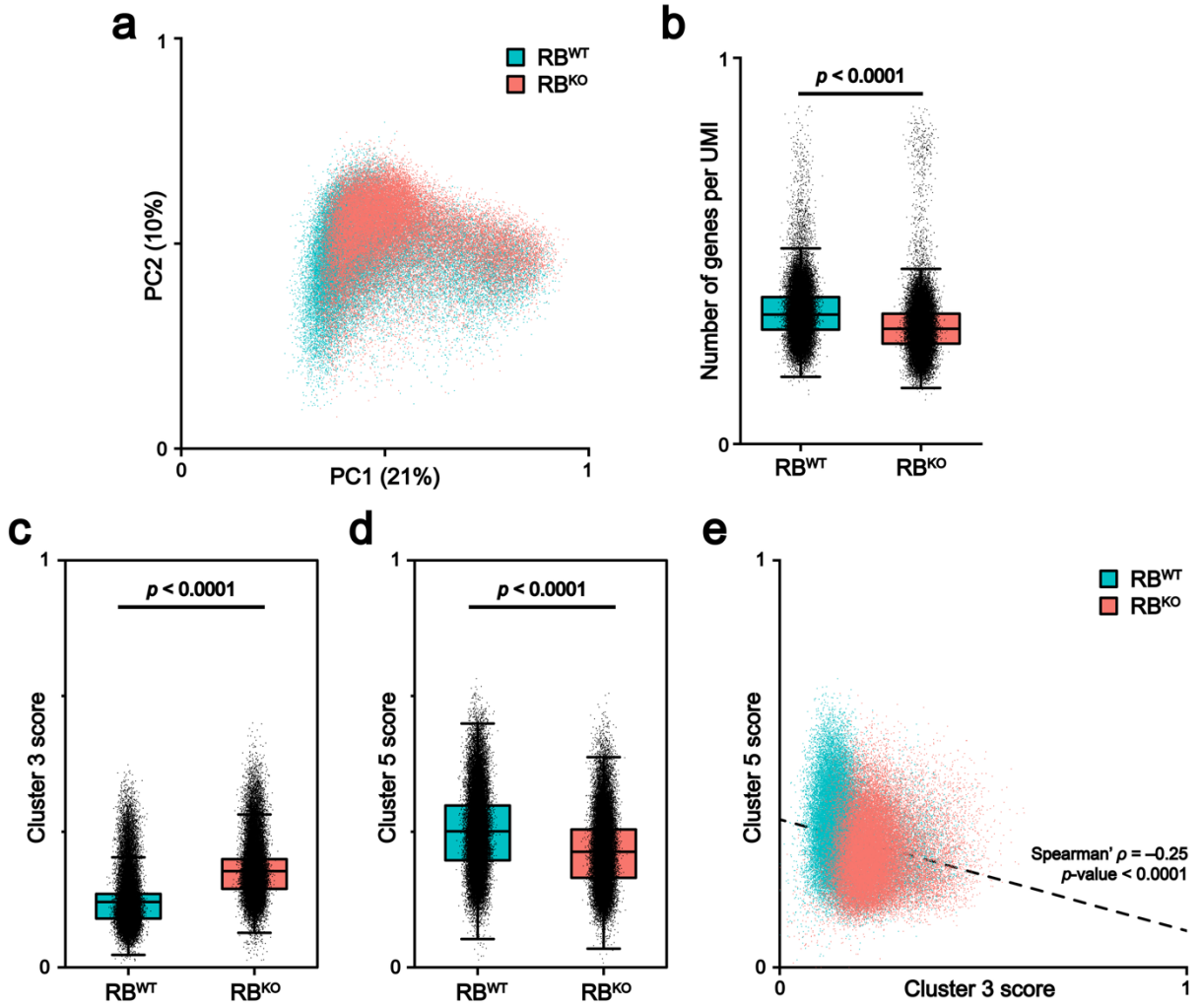

Supplementary Fig. 27. Single-cell RNA sequencing of G1-arrested RB^{WT} and RB^{KO} hTERT-RPE1 cells further validates the non-canonical RB transcriptional activation, without detecting distinct transcriptional profiles at the single-cell level.
(**a**) Principal component analysis (PCA) of single-cell transcriptomes from RB^{WT} and RB^{KO} hTERT-RPE1 cells, arrested in G1 by 6 days of contact inhibition. Each dot on the plot represents an individual cell, colored according to its genotype: RB^{WT} (cyan) and RB^{KO} (magenta). The plot visualizes the principal components (PC1 and PC2) that capture the greatest variance within the dataset. Values on the axes after the principal components indicate explained variance. (**b**) Quantification of unique gene counts per cell in G1 arrested RB^{WT} and RB^{KO} hTERT-RPE1 cells reveals that RB^{KO} cells exhibit fewer number of genes per cell compared to RB^{WT}. Gene counts were calculated by Unique Molecular Identifiers (UMI) and normalized to account for differences in sequencing depth. Box plot shows the distribution of the number of unique genes detected per cell in RB^{WT} (cyan) and RB^{KO} (magenta) hTERT-RPE1 cells. Horizontal lines indicate mean values. Statistical significance was determined by a two-tailed Student's *t*-test, $p<0.0001$****. (**c** and **d)** Average expression levels of cluster 3 and cluster 5 genes in G1 arrested RB^{WT} and RB^{KO} hTERT-RPE1 cells reveal that upon RB loss, cluster 3 genes are upregulated while cluster 5 genes are downregulated. Box plots showing the average

normalized expression levels of genes belonging to cluster 3 (c) or cluster 5 (d) in RB^{WT} (cyan) and RB^{KO} (magenta) cells. Median is indicated by the horizontal lines. Statistical significance was determined by a two-tailed Student's *t*-test, $p<0.0001$****. (**e**) Average expression levels of cluster 3 and cluster 5 genes reveal modest transcriptional shifts in RB^{KO} G1 arrested hTERT-RPE1 cells. Scatter plot visualizes the single-cell relationship between the average expression scores for genes within cluster 3 (x axis) and cluster 5 (y axis). Each dot represents an individual cell, colored by genotype; pink for RB^{WT} and maroon for RB^{KO}. A modest, but statistically significant negative Spearman correlation ($\rho= -0.25$, $p<0.0001$****) is observed between clusters 3 and 5 scores across the total population of cells, indicated by the dashed trend line. The plot annotates the inverse transcriptional regulation of these two gene sets (cluster 3 and cluster 5) at the single-cell level.

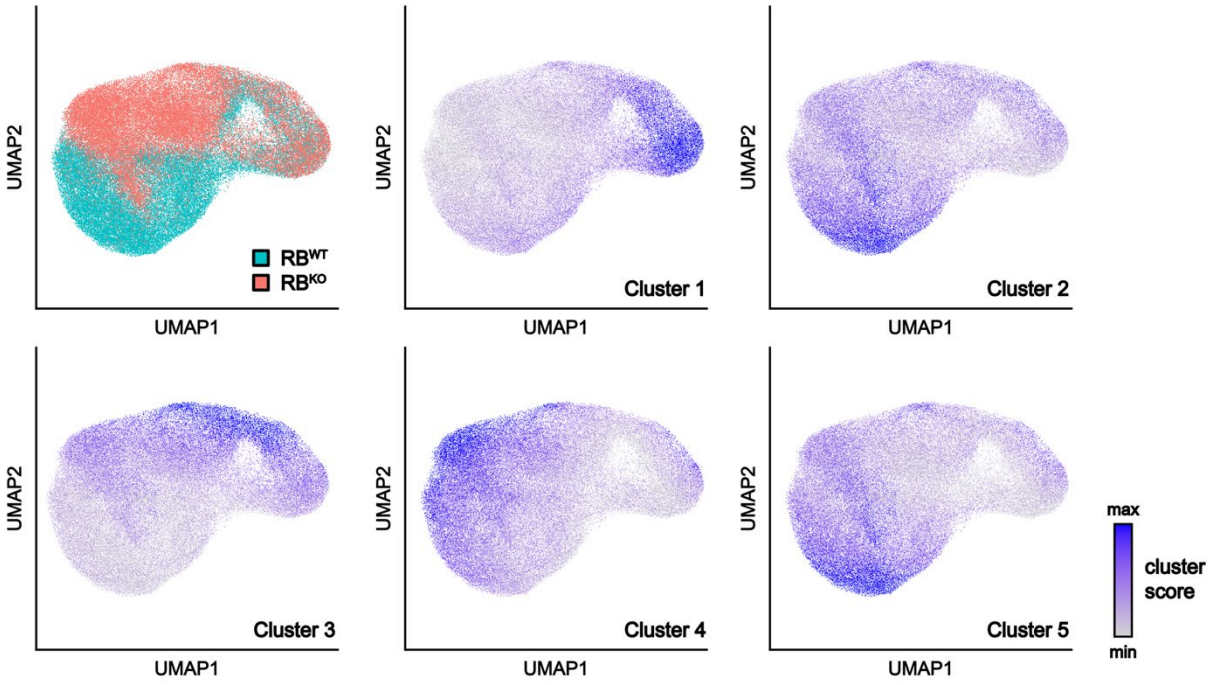

Supplementary Fig. 28. UMAP visualization of single-cell RNA sequencing of G1-arrested RB^{WT} and RB^{KO} hTERT-RPE1 cells corroborates differential transcriptional regulation by RB.

Uniform Manifold Approximation and Projection (UMAP) visualization of single-cell transcriptomes from RB^{WT} and RB^{KO} hTERT-RPE1 cells, arrested in G1 by 6 days of contact inhibition. Each dot on the plot represents an individual cell. Top left panel is colored according to its genotype: RB^{WT} (cyan) and RB^{KO} (magenta). Average expression levels of clusters 1–5 genes in G1 arrested RB^{WT} and RB^{KO} hTERT-RPE1 cells reveal that cluster 2 and cluster 5 gene expression are enhanced in RB^{WT} hTERT-RPE1 cells while cluster 3 gene expression is repressed in RB^{WT} hTERT-RPE1 cells. The plot further corroborates the inverse transcriptional regulation of cluster 3 and cluster 5 gene sets at the single-cell level.